International Journal of Heat and Fluid Flow 109 (2024) 109530

Contents lists available at ScienceDirect

International Journal of Heat and Fluid Flow

journal homepage: www.elsevier.com/locate/ijhff

Numerical and experimental investigations of diffusion-induced boundary layer separation on aero-engine nacelles

Luca Boscagli [a,*], Kshitij Sabnis [b,c], David G. MacManus [a], Holger Babinsky [b], Fernando Tejero [a], Christopher Sheaf [d]

[a] Centre for Propulsion and Thermal Power Engineering, Cranfield University, Cranfield, MK43 0AL, UK
[b] Department of Engineering, University of Cambridge, Cambridge, CB2 1PZ, UK
[c] School of Engineering and Materials Science, Queen Mary University of London, London, E1 4NS, UK
[d] Rolls-Royce plc., Derby, DE24 8BJ, UK

ARTICLE INFO

Keywords:
CFD
Windmilling
Turbofan engines
Nacelle
Validation

ABSTRACT

Aero-engine nacelles have to fulfill design requirements at both cruise and off-design conditions. Under engine windmilling conditions the ingested streamtube massflow is relatively low. A key off-design condition is take-off, which, in conjunction with an engine windmilling scenario, results in the stagnation point of the ingested streamtube being located significantly inside the intake. The combination of high angle of attack and low engine massflow rates leads to a strong flow acceleration and subsequent diffusion of the boundary layer on the upper quadrants of the external nacelle cowl, which can terminate with subsonic separation from the leading-edge. Under this condition, Reynolds number effects can play a dominant role on the separation onset and characteristics and 3D-annular wind tunnel tests cannot always achieve Reynolds' number equivalent to full scale. A novel quasi-2D rig configuration representative of the aerodynamics of a full-size aero-engine nacelle under windmilling end of runway conditions examined in detail the characteristics of the boundary layer on the external cowl of a nacelle prior to diffusion-induced separation. Separation of the boundary layer was independently promoted through changes to represent different engine massflow rates and freestream Mach number on the rig to determine the limits of steady Reynolds Averaged Navier Stokes (RANS) methods to discern the onset of boundary layer separation. For the conditions and geometry investigated, the combined experimental and computational results showed that there was laminar to turbulent transition of the boundary layer ahead of the subsonic diffusion. The work showed that steady RANS can predict the onset of boundary layer separation with an uncertainty of approximately 10% on notional engine massflow rate and 0.05 on freestream Mach number relative to a nominal operating freestream Mach number of 0.25. This provides guidance for the industrial design and optimization of future windmilling-tolerant nacelles for large ultra-high bypass ratio turbofan engines.

1. Introduction

For the aerodynamic design and optimisation of aero-engine nacelles (Tejero et al., 2019; Goulos et al., 2021; Magrini et al., 2021; Silva et al., 2022), boundary layer ingestion system (Yildirim et al., 2022) and propeller-wing configuration (Chauhan and Martins, 2021) steady Reynolds Averaged Navier Stokes (RANS) based methods are typically used. When the nacelle operates within the cruise segment of flight the boundary layer on the external cowl is typically attached and RANS methods are sufficiently reliable to predict external cowl drag (Robinson et al., 2019). However, aero-engines nacelles also need to fulfill off-design requirements where the boundary layer is prone to separation under the influence of an adverse pressure gradient (Hoelmer et al., 1987). In particular, windmilling End of Runway (EoR) conditions (Fig. 1), sometimes also referred to as second-segment take-off climb (Hoelmer et al., 1987), is a scenario where one engine is inoperative during the aircraft take-off manoeuvre, and the massflow ingested into the engine significantly reduces. Mass flow capture ratio (MFCR) is a non-dimensional aerodynamic parameter (Seddon and Goldsmith, 1999) that is defined as the ratio of the area of the ingested streamtube far upstream of the nacelle to the nacelle highlight area. Under nominal take-off conditions, this is approximately $MFCR \approx 1.5$–1.7 (Peters et al., 2015; Silva et al., 2022), and under

---

[*] Corresponding author.
E-mail address: luca.boscagli@cranfield.ac.uk (L. Boscagli).

https://doi.org/10.1016/j.ijheatfluidflow.2024.109530
Received 23 March 2024; Received in revised form 11 June 2024; Accepted 2 August 2024
Available online 15 August 2024
0142-727X/

Nomenclature

Roman Symbols

Δz_{rig}	Rig and computational domain spanwise length, [m]
h_{bump}	Bump height, [m]
k	Turbulent kinetic energy, [J/kg]
L	Length, [m]
M	Mach number, [–]
n_x, n_y, n_z	Number of grid nodes along x, y, z [–]
r	Radius, [m]
Re_t	Reynolds number based on nacelle thickness, [–]
Re_θ	Local momentum thickness Reynolds number, [–]
S_{ij}	Mean strain rate tensor, [1/s]
T	Time, [s]
t	Nacelle thickness, [m]
t_{ij}	Viscous stress tensor, [1/s]
U, V	Velocity, [m/s]
u_τ	Friction velocity, [m]
x, y, z	Coordinates, [m]
y^+	Wall distance in near-wall unit, [–]
y_w	Wall normal distance, [m]

Greek Symbols

α	Nacelle incidence angle, [°]
β	Rotta-Clauser parameter, [–]
δ	Boundary layer thickness, [m]
δ_{ij}	Kronecker delta, [–]
ϵ	Vorticity magnitude threshold, [–]
γ	Intermittency, [–]
$\hat{\tau}$	Unitary vector parallel to the nacelle wall, [–]
κ	Specific heat ratio, [–]
μ	Molecular viscosity, [kg/m/s]
ν	Kinematic viscosity, [m^2/s]
ω	Specific dissipation rate, [1/s]
$\overline{\gamma}$	Cumulative intermittency, [–]
$\overline{\omega}$	Vorticity vector, [1/s]
σ_k	Turbulent Prandtl number for k, [–]
τ_w	Wall shear stress magnitude, [Pa]
τ_x	Axial wall shear stress, [Pa]

Superscripts and Subscripts

∞	Relative to freestream
e	Relative to boundary layer outer edge
fan	Relative to aero-engine fan
i, j	Relative to tensor notation indices
in	Relative to rig inlet
L	Relative to laminar
nac	Relative to the nacelle
rig, in	Relative to rig inlet
T	Relative to turbulent
$w, wall$	Relative to nacelle wall-normal

Acronyms

EoR	End of Runway
$MFCR$	MassFlow Capture Ratio, [–]
$RANS$	Reynolds Averaged Navier Stokes
TKE	Turbulent Kinetic Energy, [J/kg]

EoR windmilling this can reduce down to $MFCR \approx 0.3$ (Hoelmer et al., 1987; Anon, 1981). The local nacelle incidence angle can be around 20° (Hoelmer et al., 1987) due to the combination of aircraft angle of attack, engine installation pitch angle and upwash due to the significant aircraft wing circulation under the take-off conditions. The take-off flight Mach number ranges from 0.2 to 0.35 (Hoelmer et al., 1987), and, under windmilling conditions, a significant flow spillage occurs around the intake lip and nacelle forebody, with a local flow acceleration subsequently followed by a significant subsonic diffusion. This can lead to large boundary layer separation starting from the nacelle leading edge (Hoelmer et al., 1987). Under windmilling conditions, the nozzle exhaust operates with low fan and core nozzle pressure ratios. In addition, when the powerplant is installed into the airframe, the presence of the wing modifies the static pressure field at the nozzle exit, which can significantly affect the exhaust mass flux (i.e., the discharge coefficient) (Goulos et al., 2023). Consequentially, under the windmilling EoR conditions there can be a further reduction in the order of 10% in the engine MFCR (Goulos et al., 2024). As a result, the stagnation point of the ingested streamtube moves further inside the aero-engine intake. Thus, the boundary layer growth length and acceleration profile around the intake lip and external forebody cowl increase. Within the context of industrial design, RANS methods still play a leading role (Slotnick et al., 2014). However, it is acknowledged that RANS based methods, either steady or unsteady, can have difficulties in determining boundary layer separation for this complex flow condition with high streamline curvature, rapid flow acceleration, followed by a strong adverse pressure gradient. Consequently, an evaluation of RANS methods, compared with new detailed experimental data, is needed for these nacelle off-design conditions where the boundary layer is prone to separation.

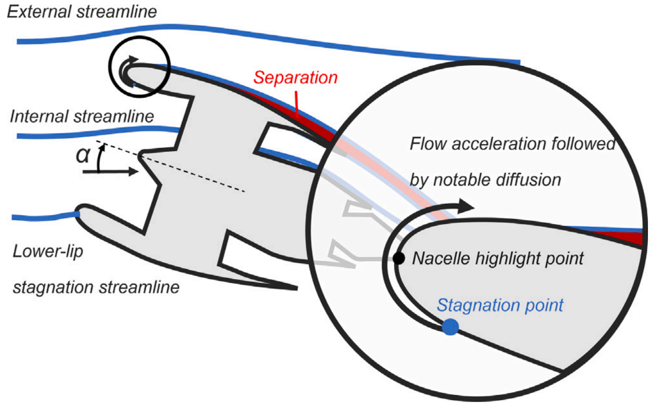

Fig. 1. Schematic the aerodynamics of an aero-engine nacelle under end-of-runway windmilling conditions.

Several recent numerical studies assessed the effect of Adverse Pressure Gradient (APG) on both attached and separating turbulent boundary layers (Vinuesa et al., 2016; Vila et al., 2017; Vinuesa et al., 2018; Wu and Piomelli, 2018; Kumar et al., 2021, 2023) and provided valuable datasets for the assessment of RANS based methods. The majority of these studies focused on the detailed analysis of changes in the mean flow and turbulence statistics due to the effect of the magnitude of the APG (Vinuesa et al., 2016), Reynolds number (Vila et al., 2017; Vinuesa et al., 2018), wall roughness (Wu and Piomelli, 2018; Kumar et al., 2021) and angle of attack (Kumar et al., 2023). The configurations investigated typically involved NACA aerofoil profiles with relatively large radius of curvature at the leading edge, and low freestream Mach number and angle of attack ($\alpha \approx 5^{\circ}$). For the detailed investigation of the incompressible characteristics of the boundary layer, wall-resolved Large Eddy Simulation were used (Vinuesa et al., 2016; Kumar et al., 2023). Both the magnitude and the streamwise distribution of the static pressure gradient have a significant impact on the characteristics of the boundary layer subject to subsonic diffusion. Experimental studies of a flat-plate turbulent boundary layer with an initial expansion and a subsequent diffusion showed that the presence of a favourable pressure gradient ahead of the diffusion leads to the development of an internal layer, which was not identified in a case which originates from a zero pressure gradient (Parthasarathy and Saxton-Fox, 2023). The internal layer is a region of strong anisotropic turbulence (Webster et al., 1996) that develops in the presence of a change in pressure gradient magnitude and polarity (Smits and Wood, 1985). Thus, the development of an internal layer presents further challenges to steady RANS methods which quite often rely on turbulence models unable to capture the anisotropy of the Reynolds stress tensor. An assessment of the reliability of linear eddy viscosity turbulence models, typically used within an industrial design framework, is needed with detailed experimental data for the specific conditions of interest (Slotnick, 2019).

In addition to this, the onset of boundary layer separation on the external nacelle cowl under EoR windmilling conditions is significantly affected by Reynolds number (Hoelmer et al., 1987). The nacelle incidence angle at which flow separation first occurs is referred here to as separation incidence angle (α_{SEP}). Based on a Reynolds number ($Re_{D_{hi}}$) defined with the nacelle highlight (Fig. 1) diameter (D_{hi}) and the freestream velocity, Hoelmer et al. (1987) showed that as the Reynolds number increases from $Re_{D_{hi}} \approx 3 \times 10^{6}$ to 7×10^{6}, α_{SEP} increases by about 5°. The maximum $Re_{D_{hi}}$ tested by Hoelmer et al. (1987) was approximately $1/3$rd of a full-size engine nacelle. The detailed status of the boundary layer was not determined, but, based on the surface isentropic Mach number (M_{ise}), it was hypothesised that at the onset of diffusion-induced separation, the boundary layer was turbulent for the range of conditions and geometries tested. However, for the next generation of ultra-high bypass ratio turbofan engines, more compact nacelles with smaller radii of curvature around the highlight may be needed to achieve fuel burn benefits at cruise (Tejero et al., 2019). Under EoR windmilling conditions, the significant flow acceleration, due to the combination of a smaller radius of curvature and the position of the stagnation point into the engine intake, could induce relaminarization of the boundary layer (Mayle, 1991). Thus, further assessment of the boundary layer characteristics on the nacelle forebody leading edge is required.

Overall, there is a need for high-quality experimental data to validate the current Computational Fluid Dynamics (CFD) methods in use within industry (Slotnick et al., 2014). Celic and Hirschel (2006) assessed through steady RANS simulations several canonical configurations (flat plate, airfoils, cylinder) with a turbulent boundary layer subject to an adverse pressure gradient. The accuracy of 11 different turbulence models was evaluated relative to experimental data for a range of freestream Mach number from 0.03 up to 0.15. None of the models outperform the others, as the accuracy of each model varied depending on the test case. Thus, it is important to assess the accuracy of the methods for the operating conditions and geometry characteristics of interest. Boscagli et al. (2024) showed that steady RANS are sufficiently accurate to predict the onset of shock-induced external cowl boundary layer separation for a nacelle under diversion windmilling conditions ($M_{\infty} \approx 0.65$, $MFCR < 0.5$, $\alpha < 5^{\circ}$). However, there is a similar requirement for a nacelle operating under windmilling EoR conditions ($M_{\infty} \approx 0.25$, $MFCR < 0.5$, $\alpha \approx 20^{\circ}$), when the separation of the boundary layer is typically driven by a subsonic, diffusion induced mechanism.

Full-scale Reynolds number tests are not always achievable even in pressurized facilities (Hoelmer et al., 1987). However, due to the notable impact of Reynolds number on boundary layers subject to subsonic adverse pressure gradient, it is important to evaluate the characteristics of the boundary layer at Reynolds numbers representative of full-size engine operating conditions. A quasi-2D rig configuration sufficiently representative of the aerodynamics of a compact aero-engine nacelle under windmilling EoR conditions was designed for this purpose (Boscagli et al., 2023). The rig provides a useful dataset to evaluate the accuracy of steady RANS methods to determine the characteristics of the boundary layer on the external cowl of an aero-engine nacelle prior to leading-edge separation (Sabnis et al., 2023). The effect of a change in notional engine massflow, freestream (or inlet) Mach number, nacelle afterbody pressure gradient and surface roughness was investigated. Making use of this set of experimental data, the purpose of this paper is to evaluate the accuracy of steady RANS methods to determine the characteristics of the boundary layer on the external cowl of a nacelle prior to separation under Reynolds number conditions which are representative of a full-size engine configuration. To the authors' knowledge, this paper presents for the first time a combined numerical and experimental assessment of the boundary layer characteristics on the external cowl of a nacelle prone to large leading-edge separation at full-size engine representative Reynolds number conditions. It is acknowledged that the influence of the azimuthal pressure gradient on the boundary layer on a 3D-annular nacelle is not captured in the quasi-2D, prismatic, rig configuration. However, this work is focused on the assessment of the separation characteristics (laminar or turbulent) under the influence of a streamwise pressure gradient, whose magnitude is sufficiently representative of a 3D-annular configuration at full-size engine Reynolds number conditions (Boscagli et al., 2023). It is believed that the azimuthal pressure gradient will not significantly change the qualitative aspects and conclusions relative to the applicability of steady RANS methods for the assessment of 3D aero-engine nacelles under windmilling end of runway conditions. In addition, the outcome of this research may set the ground for future full-3D wind tunnel tests for further CFD methods validation, which is out of the scope of this work.

The paper is structured as follows. Section 2 introduces the quasi-2D rig configuration and the experimental and numerical methodology. Section 3 presents the evaluation of the computational results with the experimental data. Section 4 presents a summary of the main conclusions of this study.

2. Rig configuration and methodology

This section briefly introduces the design intent and the experimental set up of the rig configuration that was used to assess the characteristics of the boundary layer on the external cowl of an aero-engine nacelle under end of runway windmilling conditions. A description of the computational domain and settings used is given, along with data analysis methods and computational grid resolution.

2.1. Rig design intent and limitations

The methods and design intent of the rig for the CFD methods validation for the prediction of the separation onset of the external cowl boundary layer of a nacelle operating under windmilling EoR conditions were reported in detail in Boscagli et al. (2023). However, for completeness a brief summary is also included in this manuscript to further understand the representativeness and limits of the quasi-2D rig configuration of the aerodynamics of a 3D annular nacelle at full-size engine operating conditions. The Reynolds number (Re_t) was defined based on the nacelle forebody thickness (t, Fig. 2) and rig inlet velocity (U_{in}). The choice of the lengthscale was based upon previous work (Coschignano et al., 2019), as well as the fact that it is of the same order of magnitude of the initial acceleration length

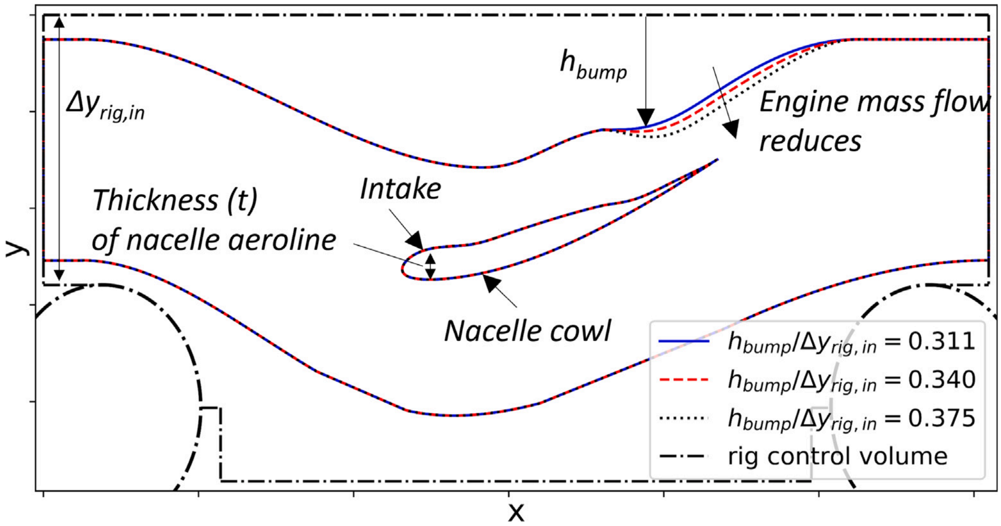

Fig. 2. Schematic of the rig configuration.

of the boundary layer around the forebody lip. Hoelmer et al. (1987) showed the importance of the boundary layer characteristics around the highlight of the nacelle, and the possibility of relaminarization due to the notable favourable pressure gradient (Mayle, 1991) also requires further investigations. The rig operated at a $Re_t \approx 1.6 \times 10^6$ (Table 1), which is sufficiently representative of the full-size engine operating conditions (Boscagli et al., 2023). An optimized 3D annular nacelle (Swarthout et al., 2022) was used to define the 2D aeroline that was then extruded along the spanwise direction and installed within the rig. The design of the bounding walls was dictated by a series of objectives and it required several trade-off studies. Firstly, the need to take into account the difference in the area distributions across the bounding streamtube due to the switch from a 3D annular configuration to a 3D prismatic (quasi-2D) one. Secondly, the need to accommodate the position of the stagnation point on the nacelle aeroline to get sufficiently representative cowl loading and streamwise pressure gradient distributions. Finally, the curvature of the bounding walls of the rig required careful manipulation to avoid separation. In addition, some portions of the bounding walls required a flatter profile to allow optical access and avoid optical distortions. This was all achieved through a combination of 3D-annular CFD studies as well as, 3D computations of the pre-test rig configuration. A set of interchangeable bump geometries was used to mimic a reduction in engine massflow rate (Fig. 2). In the following sections, each geometry is named with the ratio between the bump height (h_{bump}) and the height of the rig at the entry of the working section ($\Delta y_{rig,in}$, Fig. 2). Overall, the rig was deemed sufficiently representative of the aerodynamic of a 3D-annular nacelle at full-size engine operating conditions prior to large boundary layer separation. Upon separation of the external cowl boundary layer, it is acknowledged that in a 3D-annular configuration the azimuthal pressure gradient, as well as the fact that the flow field is not bounded by physical walls, would play a dominant role and the quasi-2D modelling approach would no longer be appropriate. However, further investigations of the post-separation regime are not within the scope of this research which is focused on the assessment of the capability of steady RANS methods to predict the onset of boundary layer separation. A further description of the rig, experimental setup and instrumentation is given in the following section.

Table 1
Nominal operating conditions of the rig at tunnel entry.

M_{in} [–]	Re_t [$\times 10^6$]	$\delta\|_{x=0}$ [mm]	$I_{\overline{U}}$ [%]
[0.2,0.35]	1.6	3–4	2.6

2.2. Experimental setup

The blow-down wind tunnel at the University of Cambridge (Sabnis et al., 2023) was configured (Fig. 3) to enable the assessment of the separation onset and characteristics of the boundary layer over a nacelle under windmilling End of Runway (EoR) conditions. To promote boundary layer separation on the nacelle external cowl, the inlet Mach number (M_{in}) was also independently increased from $M_{in} = 0.2$ to 0.35 in steps of $\Delta M_{in} = 0.05$. To characterize the flow field around the nacelle in terms of boundary layer status and characteristics, and extent of the corner flows, the rig featured conventional instrumentation, such as static pressure taps, alongside high-speed schlieren, Laser Doppler Anemometry (LDA) and Pressure Sensitive Paint (PSP). The static pressure taps were connected to a differential pressure transducer. The error on the ratio between the static pressure and the inlet total pressure was approximately $\pm 1\%$ (Sabnis et al., 2023). Relative to the isentropic Mach number, this approximately equates to an uncertainty that was below ± 0.009 and ± 0.12 around the peak and the stagnation point locations, respectively. However, for the latter the positional accuracy of the static pressure taps is more important, and this was approximately 0.075% of the nacelle length (L_{nac}). A Photron Fastcam Nova S6 camera was used for the schlieren visualizations at a frame rate of 6400 fps and an exposure time of 12 μs. The mean flow field was an average of approximately 2000 images. A faster acquisition frequency of approximately 20 000 fps was also used for instantaneous schlieren visualizations. The LDA measurements were obtained on the nacelle aeroline at mid-span ($\Delta z = 0$) at four different axial positions relative to the leading edge ($\Delta x/L_{nac} \approx 0.05$, 0.12, 0.18 and 0.24). Due to the finite size of the measurement volume, the positional accuracy of the LDA measurements normal to the wall was approximately 1/10th of the local boundary layer thickness for the thinnest profile. The absolute uncertainty on the velocity measurement was typically about $\pm 2\%$ of the local freestream velocity (Sabnis et al., 2023). The characteristics of the tunnel wall boundary layer ($\delta|_{x=0}$) and turbulence intensity ($I_{\overline{U}}$) were also measured at the entry of the working section to enable a correct representation of the effective inlet Mach number within the CFD model. A traverse Pitot probe and a single component hot-wire were used to measure the boundary layer thickness and the freestream streamwise turbulence intensity, respectively.

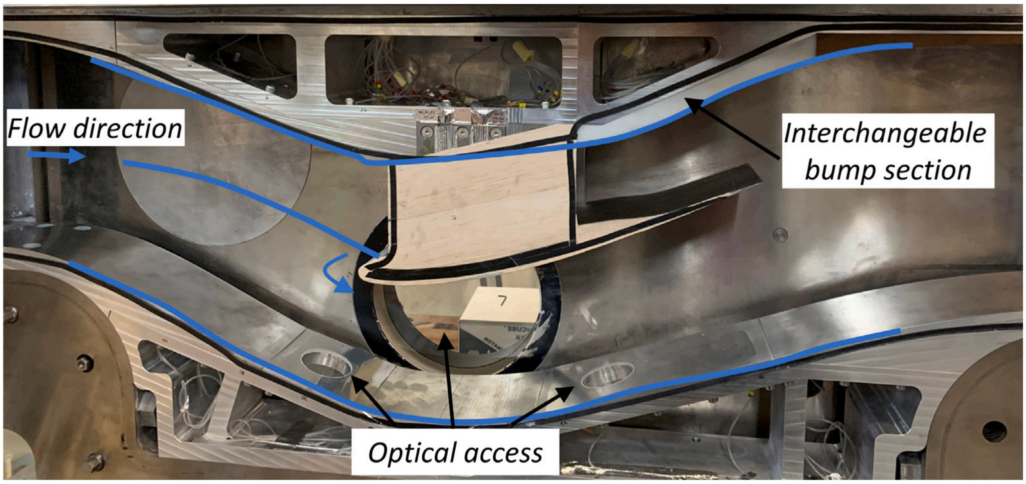

Fig. 3. Photo of the rig configuration.

2.3. Computational model

The commercial solver ANSYS Fluent version 19.1 (ANSYS Inc, 2019b) is used for the three dimensional computations presented in this work. In the followings subsections the governing equations and numerical methods used are firstly described (Section 2.3.1) and the computational domain and boundary conditions are then introduced (Section 2.3.2). The section is concluded with the data analysis methods (Section 2.3.3) and with the description of the grid characteristics and grid independence studies (Section 2.3.4).

2.3.1. Governing equations and numerical methods

The solution variables of the three dimensional, time-dependent, compressible Navier–Stokes equations for a polytropic ideal gas with density (ρ), velocity vector (u_x, u_y, u_z), and internal energy (e), are decomposed into mean ($(\tilde{\cdot})$) and fluctuating components ($(\cdot)'$) following a Reynolds-averaging decomposition and ergodic assumption. Due to the variable-density nature of the flow, the equations can be interpreted as Favre-averaged Navier–Stokes equations, with the velocities representing mass-averaged values. The conservation of mass, balance of momentum and conservation of energy can be written in Cartesian tensor form as:

$$\frac{\partial \tilde{\rho}}{\partial t} + \frac{\partial\left(\tilde{\rho}\tilde{u}_i\right)}{\partial x_i} = 0 \tag{1}$$

$$\frac{\partial\left(\tilde{\rho}\tilde{u}_i\right)}{\partial t} + \frac{\partial\left(\tilde{\rho}\tilde{u}_i\tilde{u}_j\right)}{\partial x_j} = -\frac{\partial \tilde{p}}{\partial x_j} + \frac{\partial\left(\tilde{t}_{ij} + \tilde{\rho}\tilde{\tau}_{ij}\right)}{\partial x_j} \tag{2}$$

$$\begin{aligned}\frac{\partial\left(\tilde{\rho}\left(\tilde{e} + \left(\tilde{u}_i\tilde{u}_i/2\right) + k\right)\right)}{\partial t} + \frac{\partial\left(\tilde{\rho}\tilde{u}_j\left(\tilde{h} + \left(\tilde{u}_i\tilde{u}_i/2\right) + k\right)\right)}{\partial x_j} &= \frac{\partial}{\partial x_j}\left[\tilde{u}_i\left(\tilde{t}_{ij} + \tilde{\rho}\tau_{ij}\right)\right] \\ &+ \frac{\partial}{\partial x_j}\left[\left(\frac{\mu}{Pr_L} + \frac{\mu_T}{Pr_T}\right)\frac{\partial \tilde{h}}{\partial x_j} + \left(\mu + \sigma_k\mu_T\right)\frac{\partial k}{\partial x_j}\right]\end{aligned} \tag{3}$$

$$\tilde{t}_{ij} = 2\mu\tilde{S}_{ij}, \quad \tilde{\rho}\tau_{ij} = 2\mu_T\tilde{S}_{ij} - \frac{2}{3}\tilde{\rho}k\delta_{ij}, \quad \tilde{S}_{ij} = S_{ij} - \frac{1}{3}\frac{\partial\tilde{u}_k}{\partial x_k}\delta_{ij} \tag{4}$$

In the preceding equations, h denotes the specific enthalpy, Pr_L and Pr_T are the laminar and turbulent Prandtl number, respectively, k is the turbulent kinetic energy, μ_T is the eddy viscosity, σ_k is the turbulent Prandtl number for k (Menter, 1994), t_{ij} and $\rho\tau_{ij}$ are the viscous and Reynolds stress tensor, respectively, and S_{ij} is the mean strain rate tensor, δ_{ij} is the Kronecker delta. In the rest of the manuscript, for a more concise notation, the subscript $(\tilde{\cdot})$ is dropped and capital letters are used to refer to mean (Favre-averaged) quantities. The dynamic viscosity is computed with Sutherland's law (Sutherland, 1893) , and the Prandtl number (Pr) and the specific heat ratio (κ) are set to $Pr = 0.71$ and $\kappa = 1.4$, respectively. The Reynolds stress tensor are modelled through a Boussinesq hypothesis, and the $k\omega - SST$ (Menter, 1994; Menter et al., 2003) is used as the underlying turbulence model. To assess the influence of the status of the nacelle boundary layer (laminar or fully turbulent), ahead of the subsonic diffusion, on the onset and characteristics of the boundary layer separation, both fully turbulent ($k\omega - SST$) and transitional ($\gamma - Re_\theta$, Menter et al., 2006) turbulence models were used. The calibration of the empirical coefficients appearing in the transport equations for k and for the specific dissipation rate, ω, for both turbulence models reflects the standard ANSYS Fluent version 19.1 implementation (ANSYS Inc, 2019b). The same applies to the two additional transport equations for the intermittency, γ, and momentum thickness-based Reynolds number, Re_θ, for the transitional ($\gamma - Re_\theta$) turbulence model.

The basis for the numerical method for the solution of the Favre-averaged mean conservation equations is a double-precision density-based solver with an implicit time integration formulation. A Roe flux difference splitting scheme is used for the computation of the convective fluxes and the Green-Gauss cell-based method for the computation of the gradients. The Roe scheme can be considered as second-order central difference scheme with an added matrix dissipation. A slope limiter (Barth and Jespersen, 1989) is used as a first order smoothing across flow discontinuities to prevent numerical dispersion.

2.3.2. Computational domain and boundary conditions

The modelled surfaces in the computational domain included the nacelle aeroline, the upper and lower wall of the rig, the sidewalls and the holding plates which are used to retain the nacelle within the rig (Fig. 4). The spanwise length of the domain (Δz_{rig}) is set to match the wind tunnel size, $\Delta z_{rig} = 0.114$ m. A total pressure inlet boundary conditions is used at the inlet of the CFD domain, where total pressure ($P_{0,in}$), temperature ($T_{0,in}$) and turbulence intensity ($I_{\overline{U}}$) were prescribed in agreement with what was measured in the experiments (Sabnis et al., 2023). For the turbulence quantities, in addition to $I_{\overline{U}}$, a turbulent viscosity ratio $\mu/\mu_T = 10$ was used, and for the transitional computations the intermittency value at the domain inflow was set to $\gamma = 1$ (fully turbulent flow). A static pressure outlet boundary condition with a prescribed target massflow was used at the outlet of the CFD domain, where the turbulence intensity, turbulent viscosity ratio and the intermittency, for the transitional computations, were set to $I_{\overline{U}} = 5$, $\mu/\mu_T = 10$ and $\gamma = 1$. The massflow at the outlet boundary was varied accordingly to match the nominal inlet Mach number (M_{in}) of the rig. This was inferred from the value of the static pressure measured through a static pressure tap on the sidewalls of the rig, located approximately at the tunnel mid-height and

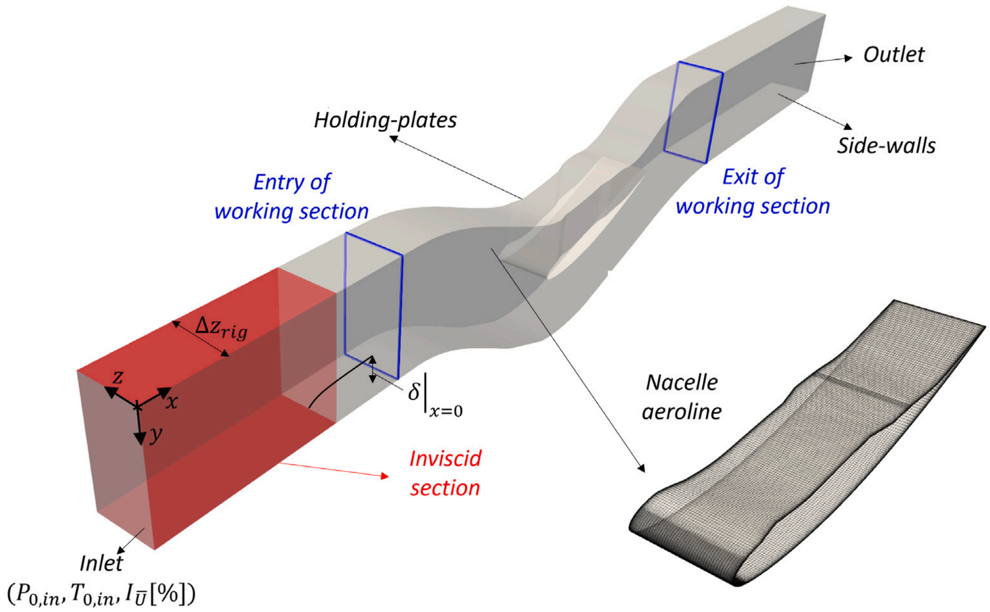

Fig. 4. Schematic of the computational domain and nacelle surface grid.

$0.09\Delta y_{rig,in}$ downstream of the entry of the working section. At that axial position within the rig, the streamline curvature imposed by the rig walls imposes a non-uniform isentropic Mach number (M_{ise}, Eq. (5)) in the vertical direction, with an overall variation of about $\Delta M_{ise} \approx 0.05$. Nevertheless, at the probe height ($y/\Delta y_{rig,in} \approx -0.48$) the isentropic Mach number closely matched the nominal inlet Mach number ($M_{in} = 0.25$). The upper and lower walls of the rig were axially extruded within the computational domain at the entry and at the exit of the working section for about twice the height of the rig inlet ($\Delta y_{rig,in}$) for numerical stability reasons. All the walls were modelled as adiabatic, hydrodynamically smooth, viscous walls, but for a region upstream of the entry of the working section which was modelled as adiabatic inviscid wall. The axial extent of this region was selected so that the height of the boundary layer at the entry of the working section matched that of the experiments (Sabnis et al., 2023, Table 1). All the CFD computations were converged to a steady state by smoothly increasing the inlet Mach number in steps of 0.025 until separation of the nacelle boundary layer. A similar approach of slowly increasing Mach number to identify the boundary layer separation condition was also adopted in the experiments. The correct representation of the massflow split within the rig and in the CFD model was further inferred a posteriori from the position of the stagnation point on the nacelle aeroline and from the isentropic Mach number distribution on the upper and lower rig walls.

$$M_{ise} = \sqrt{\frac{2}{\kappa - 1}\left[\left(\frac{P_{0,in}}{P}\right)^{\frac{\kappa-1}{\kappa}} - 1\right]} \tag{5}$$

2.3.3. Data analysis

Computational data were processed to ensure a fair comparison with experimental data, and also to further understand the nacelle boundary layer development and characteristics where experimental data could not be collected due to optical access limitations. For the evaluation with experimental data, boundary layer profiles were obtained by linearly interpolating the CFD grid data (Barber et al., 1996) and interrogating at the LDA ‘point’ measurement locations. The near-wall resolution of the CFD data was also exploited to determine the boundary layer characteristics. The streamwise velocity component (Eq. (6)) was determined and the profile numerically integrated accordingly through a trapezoidal rule. The thickness (δ) and outer edge velocity (U_e) of the boundary layer were determined based on a threshold on vorticity magnitude (ϵ, Eq. (7)) as follows,

$$U = \vec{V} \cdot \hat{\tau} \tag{6}$$

$$U = U_e \Leftrightarrow \frac{|\vec{\varpi}_e|}{|\vec{\varpi}_{y_w=0}|} \leq \epsilon \tag{7}$$

Despite the notable adverse pressure gradient, which leads to a non-equilibrium boundary layer (Vinuesa et al., 2016), the method is sufficiently robust for the Reynolds number conditions (Griffin et al., 2021) under investigation. A central differencing scheme was used to compute the velocity gradients and the vorticity field ($\vec{\varpi}$). At the boundary elements a forward/backward difference scheme was used instead. Typically, with a change in ϵ from 10^{-3} to 10^{-4}, the boundary layer characteristics were not significantly affected and therefore $\epsilon = 10^{-3}$ was used to identify the outer edge of the boundary layer.

The Rotta-Clauser (Clauser, 1954) parameter (β, Eq. (8)) was used to quantify the amount of diffusion that the boundary layer is subjected to, and β is defined as follows,

$$\beta = \frac{\delta_i^*}{\tau_w} \vec{\nabla} p_e \cdot \hat{\tau} \tag{8}$$

In Eq. (8), $\vec{\nabla} p_e$ is the pressure gradient at the boundary layer outer-edge, δ_i^* is the incompressible displacement thickness and τ_w is the magnitude of the wall shear stress. For an equilibrium turbulent boundary layer, β is constant along the streamwise direction (Vinuesa et al., 2018), and therefore β was also used to further highlight the non-equilibrium conditions of the mean boundary layer profiles on the external cowl under end of runways windmilling scenarios.

For the computations with boundary layer transition ($\gamma - Re_\theta$ turbulence model), the intermittency function (γ) was used to assess the status of the boundary layer. γ varies from $\gamma = 0$ (fully laminar) to 1 (fully turbulent). A cumulative intermittency ($\overline{\gamma}$, Eq. (9)) was used to estimate the axial position at the end of laminar to turbulent transition ($\overline{\gamma} \approx 0.99$, Gostelow et al., 1994) of the boundary layer. This was defined as the integral of intermittency in the wall normal direction (y_w), non-dimensionalized with the local boundary layer thickness ($\delta(x)$).

$$\overline{\gamma}(x) = \frac{1}{\delta(x)} \int_0^{\delta(x)} \gamma(x, y_w) d y_w \tag{9}$$

Table 2
Overall grid size and number (no.) of nodes and average resolution around the nacelle aeroline.

Grid level	Total no. nodes $[\times 10^6]$	Nodes around model $[n_x \times n_y \times n_z]$	$\Delta x/\Delta z_{rig}$ [%]	$\Delta y/\Delta z_{rig}$ [%]	$\Delta z/\Delta z_{rig}$ [%]	y^+
1	2.6	114 × 91 × 45	2	1.6	2.2	1
2	5.7	158 × 120 × 80	1.5	1.35	1.25	1
3	16.8	212 × 173 × 160	1.1	1.15	0.625	1

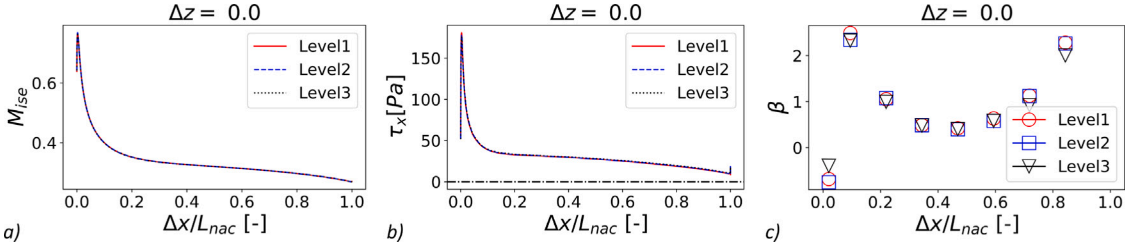

Fig. 5. Effect of grid refinement on axial distribution of (a) isentropic Mach number, (b) axial wall-shear stress and (c) Rotta-Clauser parameter on the nacelle cowl at mid-span ($\Delta z = 0$). Steady RANS computations with $k\omega - SST$ turbulence model.

The experimental flow visualization through the schlieren images where reproduced numerically by area-averaging the y component of the density gradient across seven meridional planes equispaced throughout the spanwise length (Δz_{rig}) of the computational domain. The two most offset planes relative to the rig mid-span were approximately located $0.03\Delta z_{rig}$ away from the rig side-walls.

2.3.4. Grid independence studies

A grid independence study (Celik et al., 2008) was carried out at the nominal operating conditions of the rig ($M_{in} = 0.25$, Table 1) for a configuration with no boundary layer separation on the nacelle aeroline. The grid was generated through the ANSYS ICEM software (ANSYS Inc, 2019a) and it was multi-block, fully structured with hexahedral-type elements. Three grid refinements were used and referred to as level 1, 2 and 3, respectively (Table 2). The number of grid nodes within the block around the nacelle model (n_x, n_y, n_z) was anisotropically increased and decreased relative to level 2, with an overall refinement ratio of approximately 2.5. The resolution within the boundary layer was kept approximately the same through the grids with a cell growth ratio between 1.15 and 1.2, and constant first cell height ($y_{w,1^{st}}$). Based on the friction velocity ($u_\tau = \sqrt{\tau_w/\rho}$) definition, the first cell height in non-dimensional wall unit ($y^+ = \left(\rho y_{w,1^{st}} u_\tau\right)/\mu$) was $y^+ \approx 1$. The Grid Convergence Index (GCI) for level 2 grid relative to level 3 was 0.016% when evaluated based on peak isentropic Mach number on the nacelle aeroline at mid-span ($\Delta z = 0$, Fig. 5). Relative to grid level 3, the characteristics of the boundary layer on the nacelle cowl at mid-span for level 2 were only slightly affected by the changes in outer grid resolution (Fig. 5c). Level 2 grid was considered sufficiently grid independent and the same spanwise, streamwise and wall-normal resolutions (Table 2) were used for the subsequent studies. In the presence of large boundary layer separation from the nacelle leading-edge, for some of the computations the steady RANS were not able to achieve a fully converged solution due to a significant massflow redistribution between the upper and lower channel of the rig. This is a limitation of the steady RANS approach and it was found that for those computations, in order to force convergence to a steady state solution with the same initialization strategy and global Courant–Friedrichs–Lewy (CFL) condition, it was required to switch to the finer grid (level 3), which in turn led to a local CFL that was about 3 times smaller. For those conditions a note on the figure caption is made to reflect the change in grid resolution. Nevertheless, the primary aim of this study is to identify the onset of separation of the nacelle boundary layer, and therefore the change in grid resolution for the post-separation assessment does not affect the main conclusions.

3. Results

The effect of a change in either inlet Mach number or bump height (i.e., to replicate engine massflow changes) on the characteristics of the boundary layer on the external cowl of a compact nacelle under windmilling EoR conditions was assessed in the blow-down wind tunnel of the University of Cambridge (Sabnis et al., 2023). The novel rig configuration enabled the assessment of steady RANS methods, with a particular focus on the characteristics of the boundary layer prior to separation. Post-separation, there was a significant massflow redistribution between the upper and lower channel of the rig (Boscagli et al., 2023). When this happens, due to the constraint of the rig walls, the unsteady characteristics of the boundary layer separation are no longer representative of the external flow behaviour on a full-size 3D aero-engine nacelle and therefore are not further investigated in this work. The focus of this study was up to the onset of separation.

The status (laminar/turbulent) of the boundary layer ahead of the subsonic diffusion could not be determined experimentally. Thus, this was inferred from the evaluation of fully-turbulent ($k\omega - SST$) and transitional ($\gamma - Re_\theta$) steady RANS computations alongside experimental data. Compared to experiments, for the case $h_{bump}/\Delta y_{rig,in} = 0.340$ with $M_{in} = 0.25$, both turbulence models provided good agreement in the isentropic Mach number distribution at mid-span (Fig. 6). However, while both models predicted a peak isentropic Mach number of about 1, the initial flow deceleration profile was slightly different for the two, and typically the agreement with experiments was better for the transitional ($\gamma - Re_\theta$) computations. This was associated with different boundary layer characteristics immediately downstream of the sonic peak ($\Delta x/L_{nac} \approx 0.005$, Fig. 7a,b). For the transitional computations the boundary layer at $\Delta x/L_{nac} \approx 0.005$ was still transitional ($\overline{\gamma} \approx 0.36$) and it was fully turbulent further downstream on the cowl ($\Delta x/L_{nac} > 0.015$), where there was also a peak in the strength of the adverse pressure gradient (Fig. 7c). Thus, it is argued that also in the experiments there was laminar to turbulent transition on the nacelle leading edge, due to the better agreement in the isentropic Mach number distributions for the transitional computations ($\gamma - Re_\theta$) compared to those fully turbulent ($k\omega - SST$). This was also reflected in a slightly better agreement with experiments in the boundary layer profiles in the adverse pressure gradient region (Fig. 8). For example, at $\Delta x/L_{nac} \approx 0.24$, based on a fitting of the experimental and computational data to a log-law and wake model (Sun and Childs, 1973), the boundary layer for the fully turbulent ($k\omega - SST$) and transitional ($\gamma - Re_\theta$) computations was approximately 38% and 23% thicker compared to experiments, respectively.

At the nominal inlet Mach number of $M_{in} = 0.25$, for the steady RANS computations with the transitional turbulence model ($\gamma - Re_\theta$),

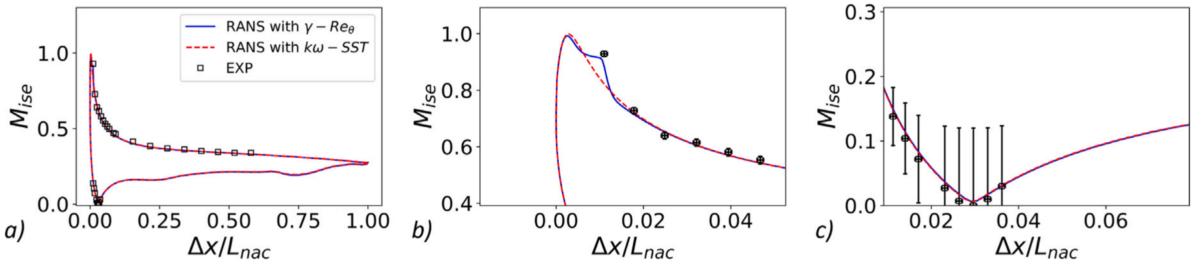

Fig. 6. Effect of turbulence model on isentropic Mach number distribution on the nacelle cowl at mid-span ($\Delta z = 0$); (b) and (c) zoom into peak M_{ise} and position of the stagnation point, respectively, and errorbars indicate the experimental uncertainty. $h_{bump}/\Delta y_{rig,in} = 0.340$, $M_{in} = 0.25$.

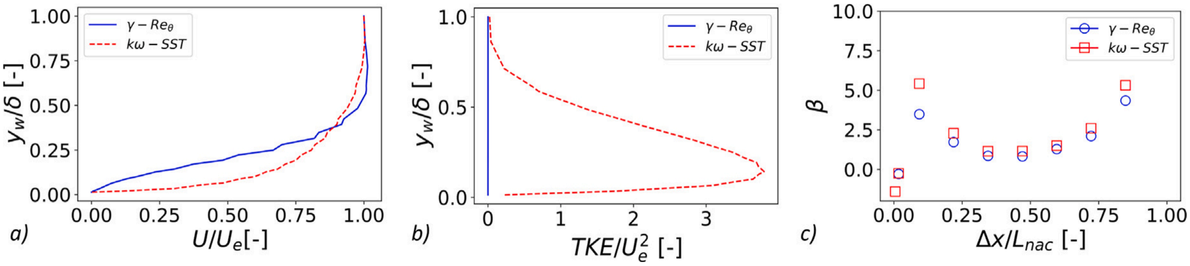

Fig. 7. Effect of turbulence model on non-dimensional (a) streamwise velocity (U) and (b) Turbulent Kinetic Energy (TKE) profiles within the boundary layer on the nacelle cowl at $\Delta x/L_{nac} \approx 0.005$ and $\Delta z = 0$; (c) effect of turbulence model on axial distribution of Rotta-Clauser parameter on the external nacelle at mid-span. $h_{bump}/\Delta y_{rig,in} = 0.340$, $M_{in} = 0.25$.

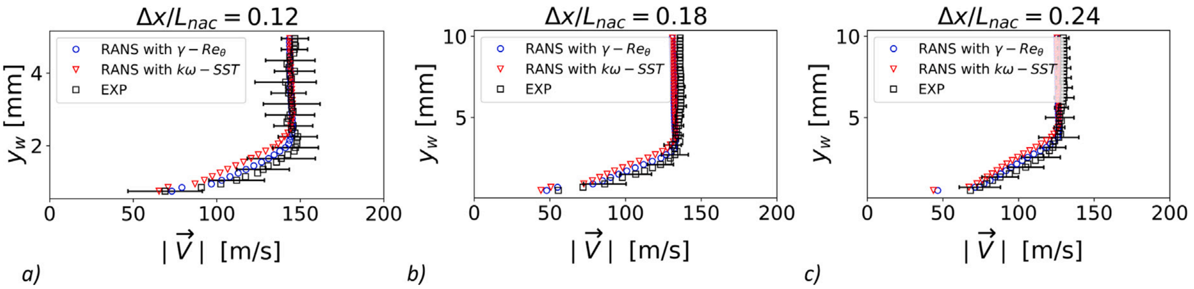

Fig. 8. Effect of turbulence model on boundary layer profiles at LDA measurements positions ($\Delta x/L_{nac} \approx 0.12$, 0.18 and 0.24) on the nacelle cowl at mid-span ($\Delta z = 0$); errorbars, plotted every 3rd point for figure readability, indicate the experimental uncertainty. $h_{bump}/\Delta y_{rig,in} = 0.340$, $M_{in} = 0.25$.

there was a laminar separation bubble on the initial forebody of the nacelle (Fig. 9). When the inlet Mach number was increased to M_{in} = 0.3, the boundary layer separation extended over the full cowl for both the fully turbulent ($k\omega - SST$) and transitional ($\gamma - Re_\theta$) boundary layer RANS computations. This indicated that, despite the local laminar separation for the transitional computations, the leading-edge boundary layer separation due to the notable adverse pressure gradient was fully turbulent. These findings related to the turbulent nature of the large diffusion induced separation confirm what was argued by Hoelmer et al. (1987). Overall, it the boundary layer remains laminar around the leading edge and transitions to turbulent further downstream on the nacelle forebody. Thus, the $\gamma - Re_\theta$ model is used in the following assessment to determine the onset and characteristics of the separation of the external cowl boundary layer. In the following sections, to improve data readability, the experimental uncertainty is omitted from the figures. However, the typical overall and local values were provided in Section 2.2.

3.1. Effect of bump height on boundary layer separation

For $M_{in} = 0.3$, it was possible to determine the effect of a change in bump height (i.e., MFCR) on the separation onset of the nacelle boundary layer. For the experiments, for the bump height $h_{bump}/\Delta y_{rig,in}$ = 0.311 and 0.340, the nacelle boundary layer was attached (Fig. 10). A further increase in bump height ($h_{bump}/\Delta y_{rig,in} = 0.375$) led to diffusion induced separation from the nacelle leading-edge. For the steady RANS calculations with the transitional turbulence model ($\gamma - Re_\theta$), the nacelle boundary layer was attached for $h_{bump}/\Delta y_{rig,in}$ = 0.311 and separated for $h_{bump}/\Delta y_{rig,in}$ = 0.340 and $h_{bump}/\Delta y_{rig,in}$ = 0.375 (Fig. 10). Based on changes in the position of the stagnation point for the quasi-2D rig configuration and a full-3D annular nacelle (Swarthout et al., 2023; Boscagli et al., 2023), it was estimated that the steady RANS computations are able to discern the onset of boundary layer separation under end-of-runway windmilling conditions with an uncertainty on massflow capture ratio of approximately 10%. Due to this difference between the steady RANS and experiments, the isentropic Mach number and boundary layer profiles were also investigated in more detail.

At the pre-separation conditions ($h_{bump}/\Delta y_{rig,in}$ = 0.311 and M_{in} = 0.3), the peak isentropic Mach number on the forebody of the nacelle was approximately $M_{ise,peak} \approx 1.3$ (Fig. 11a). The peak isentropic Mach number was approximately $M_{ise,peak} \approx 0.9$ at M_{in} = 0.25 and increased to approximately $M_{ise,peak} \approx 1.3$ at M_{in} = 0.3 (Fig. 11b), with a supersonic region formed on the nacelle forebody. Compared to $M_{in} = 0.25$, the axial extent of the laminar separation bubble on the nacelle forebody did not significantly increase (Fig. 11c). This indicates that, despite the formation of the weak shock wave at M_{in} = 0.3, the large leading-edge separation promoted by the increase in bump height (Fig. 10) is still driven by a subsonic diffusion mechanism. At the pre-separation conditions ($h_{bump}/\Delta y_{rig,in}$ = 0.311 and M_{in} = 0.3), there was good agreement for the nacelle boundary layers at $\Delta x/L_{nac}$ = 0.12 and

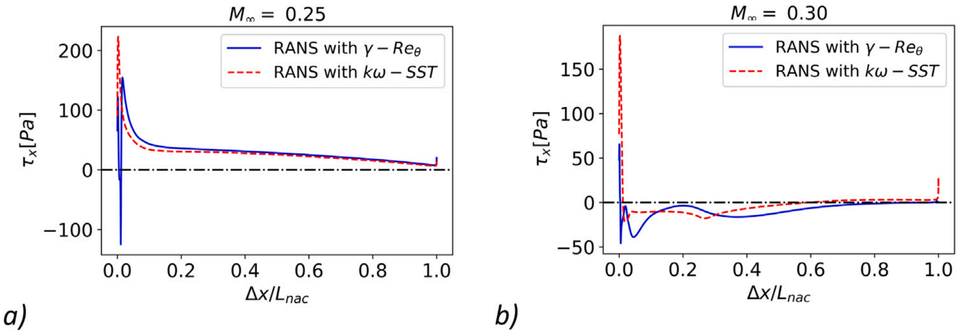

Fig. 9. Effect of turbulence model on the axial wall-shear stress (τ_x) distributions on the nacelle cowl at mid-span ($\Delta z = 0$); (a) pre- ($M_{in} = 0.25$) and (b) post ($M_{in} = 0.3$) diffusion induced separation. The black dot-dashed line distinguishes between region of attached ($\tau_x > 0$) and separated ($\tau_x < 0$) boundary layer. $h_{bump}/\Delta y_{rig,in} = 0.340$.

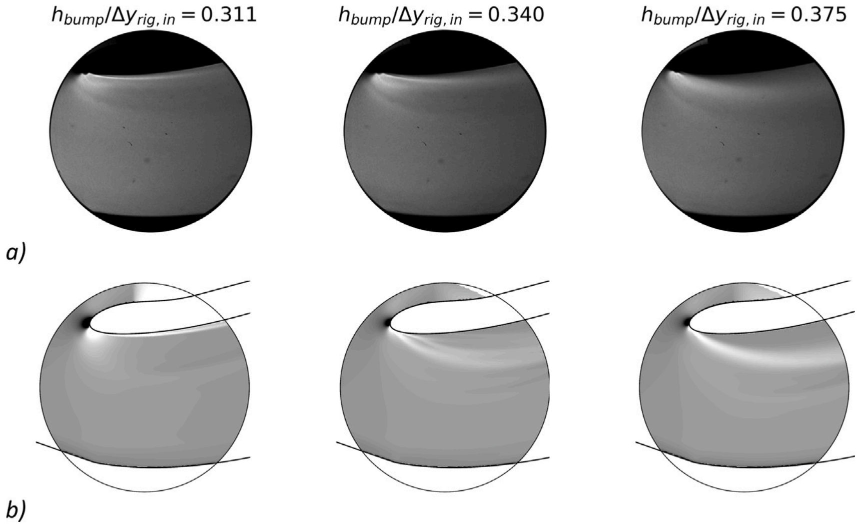

Fig. 10. Effect of bump height on the onset of nacelle boundary layer separation; (a) experimental schlieren photographs and (b) spanwise averaged density gradient ($\partial\rho/\partial y$) for the steady RANS with $\gamma - Re_\theta$ turbulence model. $M_{in} = 0.3$. In (b) the steady RANS computations at $h_{bump}/\Delta y_{rig,in} = 0.340$ were obtained with level 3 grid.

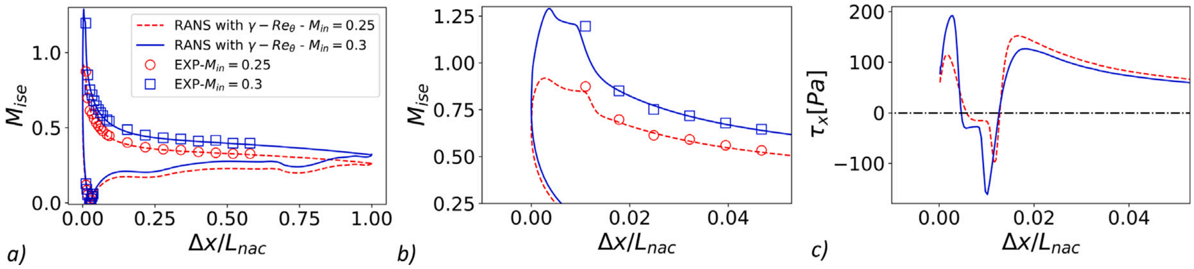

Fig. 11. (a) Effect of inlet Mach number on isentropic Mach number distribution on the nacelle cowl at mid-span ($\Delta z = 0$); (b) and (c) forebody details of M_{ise} and axial wall shear-stress distributions, respectively. $h_{bump}/\Delta y_{rig,in} = 0.311$, $M_{in} = 0.3$.

0.18 (Fig. 12). However, closer to the leading edge ($\Delta x/L_{nac} = 0.05$, Fig. 12), the steady RANS with $\gamma - Re_\theta$ turbulence model significantly overestimated the boundary layer thickness compared to experiments. This may indicate that although the boundary layer further along the nacelle is well predicted by the steady RANS, the initial effect of the strong adverse pressure gradient ($\beta \approx 7$, $\Delta x/L_{nac} \approx 0.1$) which follows the notable expansion around the leading edge ($\Delta x/L_{nac} < 0.01$) is not sufficiently well reproduced by the computations. This may explain the earlier onset of boundary layer separation for the steady RANS relative to the experiments. However, it is acknowledged that due to the small thickness of the boundary layer in the expansion region, there were no experimental data collected at that location that could enable further judgement and more firm conclusions.

3.2. Effect of inlet mach number on boundary layer separation

At a fixed bump height ($h_{bump}/\Delta y_{rig,in}$), boundary layer separation was promoted by an increase in tunnel inlet Mach number (M_{in}). Separation of the boundary layer was inferred in the experiments through evaluation of the time-averaged schlieren photographs and the static pressure measurements on the nacelle external cowl at the tunnel mid-span ($\Delta z = 0$). For example, for $h_{bump}/\Delta y_{rig,in} = 0.340$, the experiments showed an attached boundary layer on the external cowl of the nacelle for $M_{in} = 0.2$, 0.25 and 0.3 (Fig. 13a). The boundary layer thickness increased with an increase in M_{in} as depicted by the bright region on the schlieren photographs around the external cowl of the nacelle. When the inlet Mach number was further increased to $M_{in} = 0.35$, there was full cowl boundary layer separation (Fig. 13a). The steady RANS

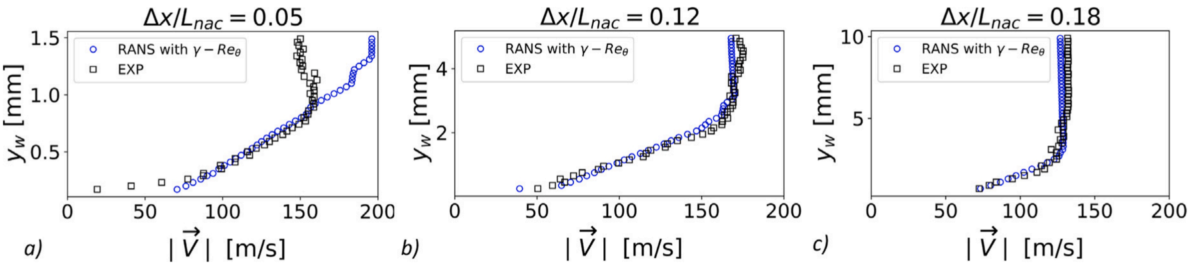

Fig. 12. Boundary layer profiles at LDA measurements positions ($\Delta x/L_{nac} \approx 0.05$, 0.12 and 0.18) on the nacelle cowl at mid-span ($\Delta z = 0$). Pre-separation conditions: $h_{bump}/\Delta y_{rig,in} = 0.311$, $M_{in} = 0.3$.

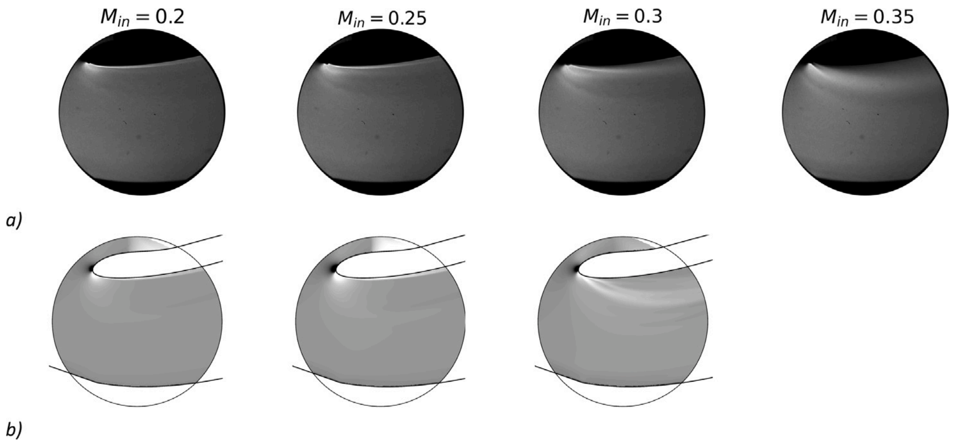

Fig. 13. Effect of inlet Mach number on the onset of nacelle boundary layer separation; (a) experimental schlieren photographs and (b) spanwise averaged density gradient ($\partial\rho/\partial y$) for the steady RANS with $\gamma - Re_\theta$ turbulence model. $h_{bump}/\Delta y_{rig,in} = 0.340$. In (b) the steady RANS computations at $M_{in} = 0.3$ were obtained with level 3 grid.

had an attached boundary layer up to $M_{in} = 0.25$. A further increase in inlet Mach number to $M_{in} = 0.3$ promoted earlier boundary layer separation compared to experiments. The computations also showed that at the attached conditions ($M_{in} = 0.25$) there were notable secondary flows developing on the upper and lower rig walls, as well as at the junction between the rig side-walls and the nacelle aeroline. Previous computational work of a similar configuration and operating conditions (Boscagli et al., 2023) showed that the rig secondary flows do not affect the onset and characteristics of the separation of the nacelle boundary layer.

When the notional MFCR was further reduced by increasing the bump height ($h_{bump}/\Delta y_{rig,in} = 0.375$), the steady RANS analyses agreed well with experiments up to $M_{in} = 0.25$ (Fig. 14). With a further increase in inlet Mach number to $M_{in} = 0.30$ there was large cowl separation in both the CFD and experiments, although the signature of the separated shear layer was more marked in the numerical schlieren compared to the experimental schlieren photos. Thus, the isentropic Mach number distributions on the nacelle external cowl at mid-span ($\Delta z = 0$) were further investigated at pre- and post-separation conditions.

For the case $h_{bump}/\Delta y_{rig,in} = 0.375$, at the pre-separation conditions ($M_{in} = 0.25$) the computations provided relatively good predictions of both the peak isentropic Mach number ($\Delta M_{ise,peak}$) and the position of the stagnation point (Fig. 15). Post-separation ($M_{in} = 0.25$), the steady RANS significantly underestimated the peak M_{ise} ($\Delta M_{ise,peak} \approx 0.2$) relative to experiments, and there were notable differences in the afterbody region (Fig. 15). Under these conditions ($M_{in} = 0.3$) the nacelle cowl boundary layer was fully separated based on the steady RANS computations. The large separated region typically led to a notable flow redistribution between the upper and lower channel of the rig, with the position of the stagnation point further upstream and closer to the nacelle leading edge (Fig. 15b at $M_{in} = 0.3$). Similarly the reduction in flow area in the lower channel, led to a notable flow acceleration. Thus, the greater M_{ise} downstream of the nacelle leading edge ($\Delta x/L_{nac} > 0.3$, Fig. 15a) for the CFD compared to experiments was likely due to a greater radial extent of the separated flow region in the computations. Overall, the steady RANS were sufficiently able to discern the onset of boundary layer separation on the external cowl, with just some minor differences on the radial extent of the separation which are likely associated with the limitations of the steady RANS approach to predict post-separation flow behaviour. As anticipated, under largely separated conditions, the rig configuration is no longer representative of the aerodynamics of a 3D-annular nacelle under end-of-runway windmilling conditions.

3.3. Effect of cowl-afterbody pressure gradient on separation onset

Previous experimental work on a 'forebody-only' configuration (Hoelmer et al., 1987) suggested that under EoR windmilling the separation of the nacelle cowl boundary layer begins from the nacelle leading-edge. Computational work on compact nacelle aerodynamics under take-off windmilling conditions (Swarthout et al., 2023) showed local separation on the nacelle afterbody which abruptly develops into full cowl boundary layer separation when the nacelle incidence angle is further increased. Thus, the separation mechanism due to the subsonic adverse pressure gradient on the external nacelle under EoR windmilling conditions was further investigated in the rig configuration. Another lower rig liner (Fig. 16) was designed to assess the effect of afterbody pressure gradient on the separation onset and characteristics of the boundary layer on the external nacelle cowl. In the following paragraphs, the two configurations are referred to as baseline and modified, respectively. Following the design intent, the configuration with the modified lower liner featured about 50% lower strength of the adverse pressure gradient (β) on the nacelle afterbody ($\Delta x/L_{nac} > 0.75$, Fig. 17) relative to the baseline. At a fixed bump height ($h_{bump}/\Delta y_{rig,in} = 0.340$), the inlet Mach number was progressively increased to promote boundary layer separation.

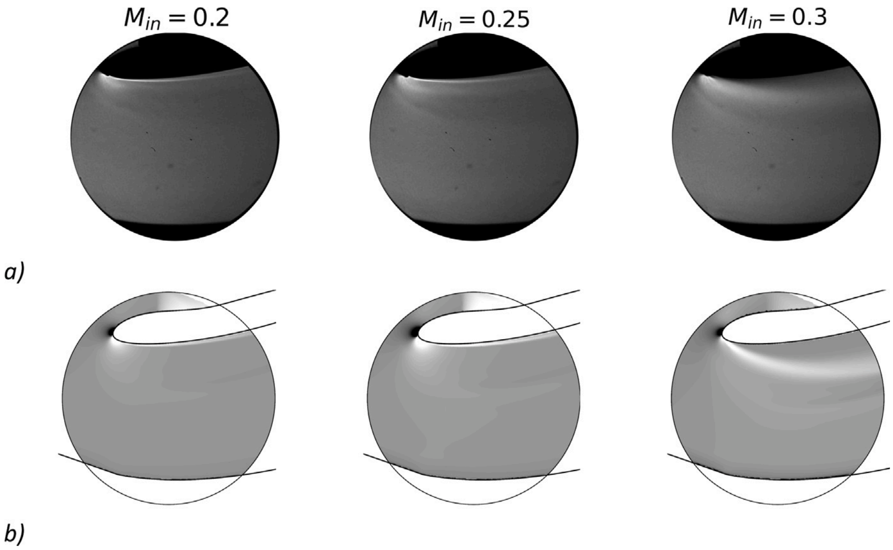

Fig. 14. Effect of inlet Mach number on the onset of nacelle boundary layer separation; (a) experimental schlieren photographs and (b) spanwise averaged density gradient ($\partial\rho/\partial y$) for the steady RANS with $\gamma - Re_\theta$ turbulence model. $h_{bump}/\Delta y_{rig,in} = 0.375$.

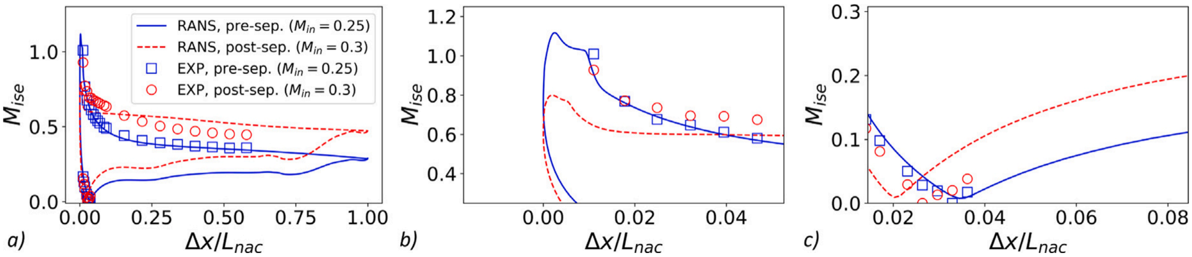

Fig. 15. Isentropic Mach number distribution on the nacelle cowl at mid-span ($\Delta z = 0$) pre and post nacelle boundary layer separation; (b) and (c) zoom into peak M_{ise} and position of the stagnation point, respectively. $h_{bump}/\Delta y_{rig,in} = 0.375$.

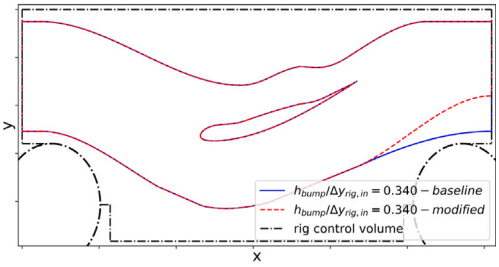

Fig. 16. Schematic of rig configuration with baseline and modified lower wall.

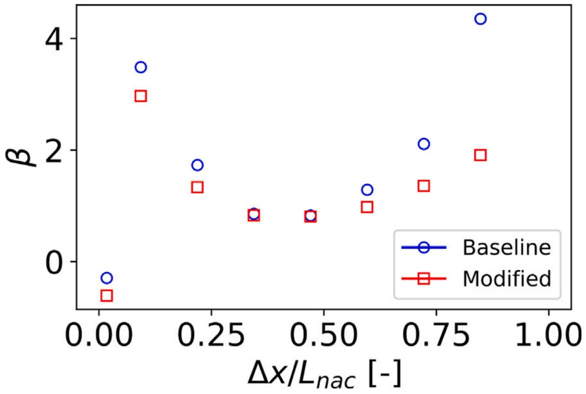

Fig. 17. Effect of lower rig wall on the axial distribution of Rotta-Clauser pressure gradient parameter on the nacelle external cowl at mid-span ($\Delta z = 0$). $h_{bump}/\Delta y_{rig,in} = 0.340$, $M_{in} = 0.25$. Steady RANS with $\gamma - Re_\theta$ turbulence model.

In the experiments, the strength of the adverse pressure gradient on the cowl afterbody did not affect the separation onset and characteristics of the nacelle boundary layer (Fig. 18). For the baseline and the modified case, the boundary layer was attached at $M_{in} = 0.25$ and 0.3, and there was leading-edge diffusion induced separation at $M_{in} = 0.35$ as indicated by the plateaux in the M_{ise} distribution on the nacelle external cowl (Fig. 18c) and further confirmed by the time-average schlieren photographs (Fig. 19). At the pre-separation conditions, the change in the lower rig wall did not significantly affect the position of the stagnation point on the intake, which indicates that the massflow split within the rig was similar. Based on the steady RANS computations with $\gamma - Re_\theta$ turbulence model, the critical inlet Mach number ($M_{in,c}$) at which separation first occurs was only slightly delayed for the modified wall, $M_{in,c} = 0.35$ (Fig. 18c), compared to the baseline configuration, $M_{in,c} = 0.3$ (Fig. 18b). This is further confirmation that the separation is driven by a subsonic diffusion starting from the leading edge of the nacelle (Fig. 19), and the afterbody pressure gradient only slightly affected the separation onset predicted by the steady RANS computations with the $\gamma - Re_\theta$ turbulence model.

4. Conclusions

The novelty of this work is the numerical and experimental investigation of a quasi-2D rig configuration which was sufficiently representative of the aerodynamics of a nacelle under end-of-runway

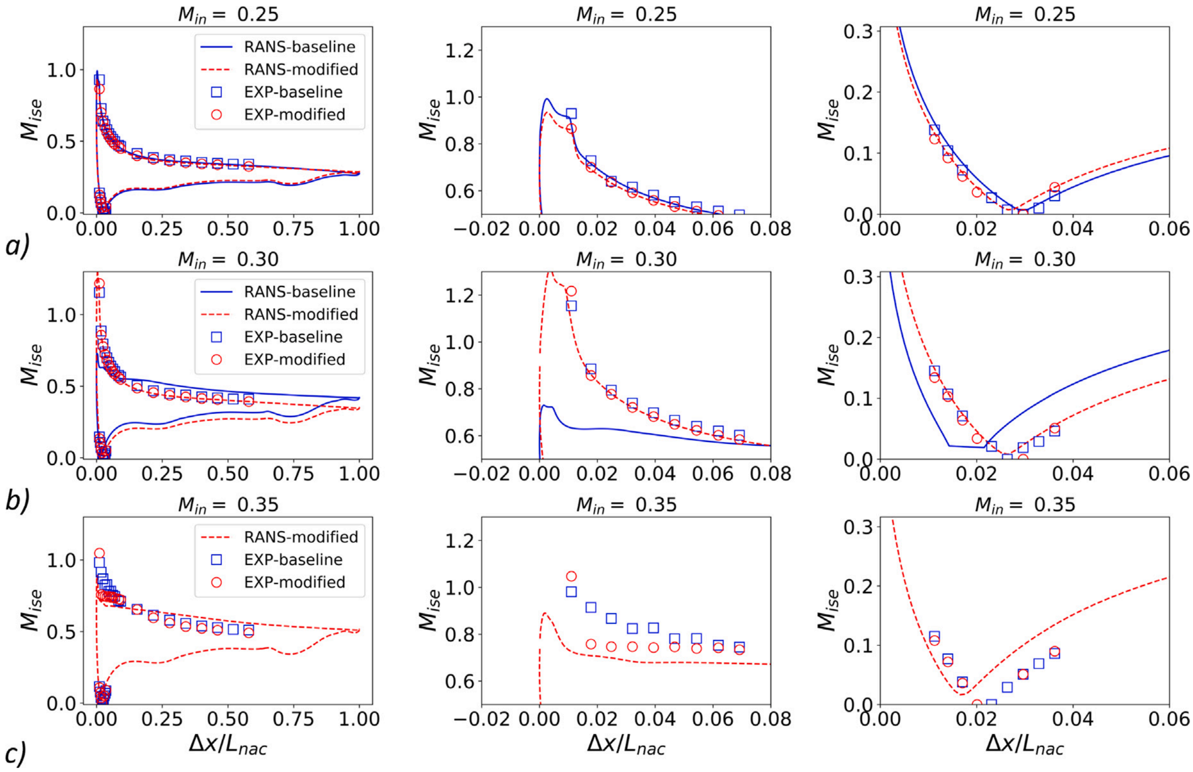

Fig. 18. Effect of lower rig wall on the isentropic Mach number distribution on the nacelle aeroline at mid-span ($\Delta z = 0$) for the case with $h_{bump}/\Delta y_{rig,in} = 0.340$. (a) $M_{in} = 0.25$, (b) $M_{in} = 0.3$ and (c) $M_{in} = 0.35$.

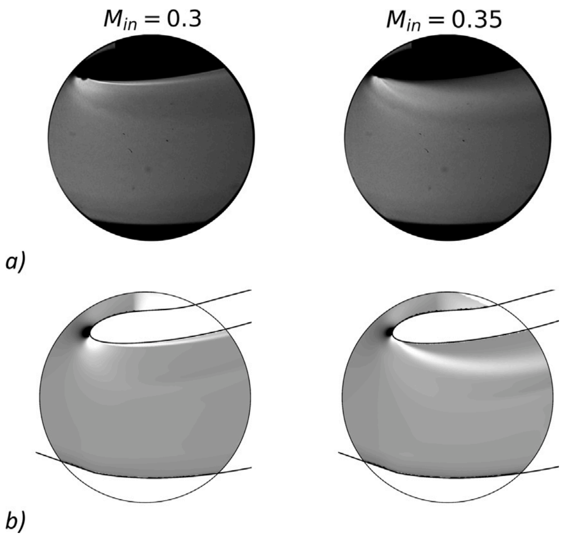

Fig. 19. Effect of inlet Mach number on the onset of nacelle boundary layer separation; (a) experimental schlieren photographs and (b) spanwise averaged density gradient ($\partial\rho/\partial y$) for the steady RANS with $\gamma - Re_\theta$ turbulence model. 'Modified' configuration with $h_{bump}/\Delta y_{rig,in} = 0.340$.

windmilling conditions. The rig configuration enabled the assessment of the boundary layer characteristics prior to separation, which have a notable impact on the separation incidence angle of the nacelle. The combination of computational and experimental investigations showed that for a full-size engine nacelle under end-of-runway windmilling conditions the boundary layer on the nacelle leading edge is likely to be laminar and there is transition to turbulence further along the forebody. However, at the onset of large diffusion induced separation, the boundary layer is fully turbulent. Overall, compared to experiments, the steady RANS with the transitional turbulence model typically predicted an earlier onset of boundary layer separation. The steady RANS calculations, with $\gamma - Re_\theta$ turbulence model, are able to determine the onset of boundary layer separation on the external nacelle cowl with an uncertainty of $\Delta M_{in} = 0.05$, relative to a nominal $M_{in} = 0.25$, and of approximately 10% on MFCR. The strength of the pressure gradient on the afterbody of the nacelle did not affect the onset of separation in the experiments, and this was only slightly delayed in the steady RANS computations. This indicated that the separation of the boundary layer from the nacelle leading edge was driven by the subsonic adverse pressure gradient on the nacelle forebody. Overall, the contribution of this research is to quantify, for the first time, the performance of typical industrial computational methods used for the design and optimization of windmilling-tolerant aero-engine nacelles. It is believed that the high quality of the experimental measurements, which captured the thin boundary layer profiles, and the use of the steady RANS computations to further corroborate the experimental results and provide more insight into the status of the boundary layer near the nacelle leading edge, provide a good foundation for subsequent studies using eddy-resolving models that will investigate the detailed transient and complex nature of the separated boundary layer. This will help to push further the design boundaries of future compact nacelle configurations for ultra-high bypass ratio aero-engines.

CRediT authorship contribution statement

Luca Boscagli: Writing – review & editing, Writing – original draft, Visualization, Validation, Methodology, Formal analysis, Data curation, Conceptualization. **Kshitij Sabnis:** Writing – review & editing, Methodology, Investigation, Formal analysis, Data curation, Conceptualization. **David G. MacManus:** Writing – review & editing, Supervision, Project administration, Funding acquisition, Conceptualization. **Holger Babinsky:** Supervision, Resources, Funding acquisition, Conceptualization.

Fernando Tejero: Methodology, Funding acquisition, Conceptualization. **Christopher Sheaf:** Writing – review & editing, Supervision, Project administration, Conceptualization.

Declaration of competing interest

The authors declare that they have no known competing financial interests or personal relationships that could have appeared to influence the work reported in this paper.

Data availability

The data that has been used is confidential.

Acknowledgements

This project has received funding from the Clean Sky 2 Joint Undertaking (JU) under grant agreement number 101007598. The JU receives support from the European Union's Horizon 2020 research and innovation programme and the Clean Sky 2 JU members other than the Union.

References

Anon, 1981. Estimation of windmilling drag and airflow of Turbo-Jet and Turbo-Fan engines. Eng. Sci. Data Unit Data Items (76034).

ANSYS Inc, 2019a. ANSYS ICEM CFD Tutorial Manual. Technical Report, Canonsburg, PA, p. 15317.

ANSYS Inc, 2019b. ANSYS FLUENT Theory Guide. Technical Report, Canonsburg, PA, p. 15317.

Barber, C. Bradford., Dobkin, David. P., Huhdanpaa, Hannu., 1996. The quickhull algorithm for convex hulls. ACM Trans. Math. Softw. 22 (4), 469–483.

Barth, Timothy., Jespersen, Dennis., 1989. The design and application of upwind schemes on unstructured meshes. In: AIAA 27th Aerospace Sciences Meeting. http://dx.doi.org/10.2514/6.1989-366, 366.

Boscagli, Luca., MacManus, David., Tejero, Fernando., Sabnis, Kshitij., Babinsky, H., Sheaf, Christopher T., 2024. Characteristics of shock-induced boundary-layer separation on nacelles under windmilling diversion conditions. AIAA J. 62 (1), 79–91. http://dx.doi.org/10.2514/1.J063209.

Boscagli, Luca., Tejero, Fernando., Swarthout, Avery. E., MacManus, David. G., Sabnis, Kshitij., Babinsky, Holger., Sheaf, Christopher., 2023. Design of a quasi-2d rig configuration to assess nacelle aerodynamics under windmilling conditions. In: AIAA AVIATION 2023 Forum. p. 3392. http://dx.doi.org/10.2514/6.2023-3392.

Celic, Alan., Hirschel, Ernst H., 2006. Comparison of eddy-viscosity turbulence models in flows with adverse pressure gradient. AIAA J. 44 (10), 2156–2169. http://dx.doi.org/10.2514/1.14902.

Celik, Ismail B., Ghia, Urmila., Roache, Patrick J., Freitas, Christopher J., Coleman, Hugh., Raad, Peter E., 2008. Procedure for estimation and reporting of uncertainty due to discretization in CFD applications. ASME J. Fluids Eng. Trans. (ISSN: 00982202) 130 (7), 0780011–0780014. http://dx.doi.org/10.1115/1.2960953.

Chauhan, Shamsheer S., Martins, Joaquim R.R.A., 2021. Rans-based aerodynamic shape optimization of a wing considering propeller–wing interaction. J. Aircr. 58 (3), 497–513. http://dx.doi.org/10.2514/1.C035991.

Clauser, Francis. H., 1954. Turbulent boundary layers in adverse pressure gradients. J. Aeronaut. Sci. 21 (2), 91–108.

Coschignano, A., Atkins, N., Babinsky, H., Serna, J., 2019. Effect of Reynolds number on a normal shock wave-transitional boundary-layer interaction over a curved surface. Exp. Fluids (ISSN: 14321114) 60 (12), 1–12. http://dx.doi.org/10.1007/s00348-019-2824-0.

Gostelow, J.P., Blunden, A.R., Walker, G.J., 1994. Effects of free-stream turbulence and adverse pressure gradients on boundary layer transition. J. Turbomach. (ISSN: 0889-504X) 116 (3), 392–404. http://dx.doi.org/10.1115/1.2929426.

Goulos, Ioannis., MacManus, David G., Rebassa, Josep. Hueso., Alderman, James., Christopher, T. J. Sheaf, 2024. Impact of installation on the performance of a civil turbofan exhaust at wind-milling: A combined experimental and numerical approach. Aerosp. Sci. Technol. Under journal review.

Goulos, Ioannis., MacManus, David G., Rebassa, Josep. Hueso., Tejero, Fernando., Au, Andy., Christopher, T. J. Sheaf, 2023. Impact of installation on the performance of an aero-engine exhaust at wind-milling flow conditions. J. Eng. Gas Turbines Power (ISSN: 0742-4795) 10, 1–28. http://dx.doi.org/10.1115/1.4063939.

Goulos, Ioannis., Otter, John., Tejero, Fernando., Rebassa, Josep. Hueso., MacManus, David., Sheaf, Christopher., 2021. Civil turbofan propulsion aerodynamics: Thrust-drag accounting and impact of engine installation position. Aerosp. Sci. Technol. (ISSN: 12709638) 111, 106533. http://dx.doi.org/10.1016/j.ast.2021.106533.

Griffin, Kevin. Patrick., Fu, Lin., Moin, Parviz., 2021. General method for determining the boundary layer thickness in nonequilibrium flows. Phys. Rev. Fluids 6 (2), 024608.

Hoelmer, Werner., Younghans, James L., Raynal, Jean. Claude., 1987. Effect of Reynolds number on upper cowl flow separation. J. Aircr. (ISSN: 00218669) 24 (3), 161–169. http://dx.doi.org/10.2514/3.45411.

Kumar, Vishal., Miró, Arnau., Lehmkuhl, Oriol., Piomelli, Ugo., 2023. Flow separation in airfoils with rough leading edges. AIAA J. (ISSN: 1533385X) 61 (5), 2035–2047. http://dx.doi.org/10.2514/1.J062427.

Kumar, Vishal., Piomelli, Ugo., Lehmkuhl, Oriol., 2021. Large-eddy simulations of the flow on an aerofoil with leading-edge imperfections. J. Turbul. (ISSN: 14685248) 22 (11), 735–760. http://dx.doi.org/10.1080/14685248.2021.1973015.

Magrini, Andrea., Buosi, Denis., Benini, Ernesto., 2021. Maximisation of installed net resulting force through multi-level optimisation of an ultra-high bypass ratio engine nacelle. Aerosp. Sci. Technol. 119, 107169.

Mayle, Robert. Edward., 1991. The role of laminar-turbulent transition in gas turbine engines. J. Turbomach. (ISSN: 15288900) 113 (4), 509–536. http://dx.doi.org/10.1115/1.2929110.

Menter, F.R., 1994. Two-equation eddy-viscosity turbulence models for engineering applications. AIAA J. 32 (8), 1598–1605. http://dx.doi.org/10.2514/3.12149.

Menter, Florian. R., Kuntz, Martin., Langtry, Robin., 2003. Ten years of industrial experience with the SST turbulence model. Turbul. Heat Mass Transf. 4 (1), 625–632.

Menter, F.R., Langtry, R.B., Likki, S.R., Suzen, Y.B., Huang, P.G., Völker, S., 2006. A correlation-based transition model using local variables - part I: Model formulation. J. Turbomach. (ISSN: 0889504X) 128 (3), 413–422. http://dx.doi.org/10.1115/1.2184352.

Parthasarathy, Aadhy., Saxton-Fox, Theresa., 2023. A family of adverse pressure gradient turbulent boundary layers with upstream favourable pressure gradients. J. Fluid Mech. 966, A11. http://dx.doi.org/10.1017/jfm.2023.429.

Peters, Andreas., Spakovszky, Zoltán. S., Lord, Wesley. K., Rose, Becky., 2015. Ultrashort nacelles for low fan pressure ratio propulsors. J. Turbomach. (ISSN: 15288900) 137 (2), http://dx.doi.org/10.1115/1.4028235.

Robinson, Matthew., MacManus, David. G., Sheaf, Christopher., 2019. Aspects of aero-engine nacelle drag. Proc. Inst. Mech. Eng. G 233 (5), 1667–1682.

Sabnis, Kshitij., Boscagli, Luca., Babinsky, Holger., MacManus, David G., Sheaf, Christopher., 2023. Experimental investigation of external fan cowl separation for compact nacelles in windmilling scenarios. In: AIAA AVIATION 2023 Forum. http://dx.doi.org/10.2514/6.2023-3394.

Seddon, J., Goldsmith, E.L., 1999. Intake Aerodynamics, vol. 2, Blackwell Science Oxford.

Silva, Vinícius T., Lundbladh, Anders., Petit, Olivier., Xisto, Carlos., 2022. Multipoint aerodynamic design of ultrashort nacelles for ultrahigh-bypass-ratio engines. J. Propuls. Power 1–18. http://dx.doi.org/10.2514/1.b38497.

Slotnick, Jeffrey.P., 2019. Integrated CFD validation experiments for prediction of turbulent separated flows for subsonic transport aircraft. In: NATO Science and Technology Organization Proceedings RDP. STO-MP-AVT-307,.

Slotnick, Jeffrey. P., Khodadoust, Abdollah., Alonso, Juan., Darmofal, David., Gropp, William., Lurie, Elizabeth., Mavriplis, Dimitri. J., 2014. CFD Vision 2030 Study: A Path To Revolutionary Computational Aerosciences. Technical Report CR-2014-218178,, NASA.

Smits, A.J., Wood, D.H., 1985. The response of turbulent boundary layers to sudden perturbations. Annu. Rev. Fluid Mech. 17 (1), 321–358.

Sun, Chen-Chih., Childs, Morris. E., 1973. A modified wall wake velocity profile for turbulent compressible boundary layers. J. Aircraft 10 (6), 381–383.

Sutherland, William, 1893. Lii the viscosity of gases and molecular force. Lond. Edinb. Dublin Philos. Mag. J. Sci. 36 (223), 507–531. http://dx.doi.org/10.1080/14786449308620508.

Swarthout, Avery E., MacManus, David G., Tejero, Fernando., García, Jesús. Matesanz., Goulos, Ioannis., Boscagli, Luca., Sheaf, Christopher., 2023. Aerodynamics of a compact nacelle at take-off conditions. In: AIAA AVIATION 2023 Forum. p. 3309. http://dx.doi.org/10.2514/6.2023-3309.

Swarthout, Avery., MacManus, David., Tejero, Fernando., Matesanz-García, Jesús., Boscagli, Luca., Sheaf, Christopher., 2022. A Comparative Assessment of Multi-Objective Optimisation Methodologies for Aero-Engine Nacelles, vol. 09, ICAS.

Tejero, Fernando., Robinson, Matthew., MacManus, David G., Sheaf, Christopher., 2019. Multi-objective optimisation of short nacelles for high bypass ratio engines. Aerosp. Sci. Technol. (ISSN: 12709638) 91, 410–421. http://dx.doi.org/10.1016/j.ast.2019.02.014.

Vila, Carlos. Sanmiguel., Örlü, Ramis., Vinuesa, Ricardo., Schlatter, Philipp., Ianiro, Andrea., Discetti, Stefano., 2017. Adverse-pressure-gradient effects on turbulent boundary layers: Statistics and flow-field organization. Flow Turbul. Combust. 99 (3–4), 589–612. http://dx.doi.org/10.1007/s10494-017-9869-z.

Vinuesa, R., Bobke, A., Örlü, R., Schlatter, P., 2016. On determining characteristic length scales in pressure-gradient turbulent boundary layers. Phys. Fluids (ISSN: 10897666) 28 (5), http://dx.doi.org/10.1063/1.4947532.

Vinuesa, R., Negi, P.S., Atzori, M., Hanifi, A., Henningson, D.S., Schlatter, P., 2018. Turbulent boundary layers around 612 wing sections up to rec=1,000,000. Int. J. Heat Fluid Flow (ISSN: 0142727X) 72, 86–99. http://dx.doi.org/10.1016/j.ijheatfluidflow.2018.04.017.

Webster, D.R., DeGraaff, D.B., Eaton, J.K., 1996. Turbulence characteristics of a boundary layer over a two-dimensional bump. J. Fluid Mech. 320, 53–69.

Wu, Wen., Piomelli, Ugo., 2018. Effects of surface roughness on a separating turbulent boundary layer. J. Fluid Mech. (ISSN: 14697645) 841, 552–580. http://dx.doi.org/10.1017/jfm.2018.101.

Yildirim, Anil., Gray, Justin S., Mader, Charles A., Martins, Joaquim R.R.A., 2022. Boundary-layer ingestion benefit for the starc-abl concept. J. Aircr. 59 (4), 896–911. http://dx.doi.org/10.2514/1.C036103.